International Journal of Analytical, Experimental and Finite Element Analysis
Volume 13, Issue 2, June 2026, pp 88 - 100
https://doi.org/10.26706/ijaefea.13.2.20260405

Dynamic Analysis and ANN based Optimization of Thermally Stressed Rotating High-Pressure Compressor Blades

Amarjeet Banjare[1], Uttam Kumar Kar[2*]

[1]Research Scholar, Mechanical Engineering Department, CCET, Bhilai-490026, Chhattisgarh,
[2]Assistant Professor, Mechanical Engineering Department, CCET, Bhilai-490026, Chhattisgarh,

*Correspondence: ukkar093 @gmail.com

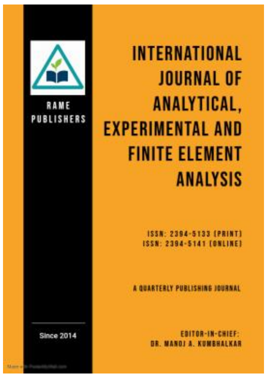

Article – Peer Reviewed
Received: 12 April 2026
Accepted: 17 June 2026
Published: 27 June 2026

Cite this article: Amarjeet Banjare, Uttam Kumar Kar, "Dynamic Analysis and ANN based Optimization of Thermally Stressed Rotating High-Pressure Compressor Blades", *International Journal of Analytical, Experimental and Finite Element Analysis*, RAME Publishers, vol. 13, issue 2, pp. 88-100, 2026.
https://doi.org/10.26706/ijaefea.13.2.20260405

Abstract: High-pressure compressor blades in aero-engines operate under severe thermo-mechanical environments characterized by high rotational speeds, elevated temperatures, and dynamic loading. Accurate prediction and optimization of their vibration behavior are essential for ensuring structural reliability and preventing resonance-induced failures. In this study, a high-pressure compressor blade is modeled as a thermally stressed rotating tapered beam, and its dynamic behavior is investigated using finite element analysis. The effects of rotational speed, temperature rise, material gradation, and aspect ratio on natural frequency and dynamic deflection are examined. A feed-forward Artificial Neural Network (ANN) is developed to predict vibration responses using finite element-generated datasets. The trained ANN model is subsequently integrated with Particle Swarm Optimization (PSO) and Multi-Objective Particle Swarm Optimization (MOPSO) algorithms to maximize natural frequency and minimize dynamic deflection simultaneously. Results indicate that rotational speed increases structural stiffness through centrifugal stiffening, while temperature rise reduces stiffness and vibration resistance. The ANN model predicts vibration characteristics with less than 5% error compared to finite element results. Optimization results demonstrate a significant improvement in natural frequency and vibration suppression, confirming the effectiveness of the proposed ANN-assisted optimization framework for rotating compressor blade design.

Keywords: Compressor blade, Rotating beam, Free vibration, Artificial Neural Network, Optimization, Thermo-mechanical loading.

1. Introduction

Rotating structural components, such as turbine blades, helicopter rotors, industrial shafts, and satellite appendages, are ubiquitous in modern engineering systems [1–3]. Their operational integrity and performance are profoundly influenced by their vibrational characteristics. Understanding and accurately predicting the dynamic behavior of these components is paramount for ensuring their structural reliability, preventing catastrophic failures, and optimizing their operational lifespan. This is particularly crucial when these components are subjected to extreme environmental conditions, such as high temperatures, which are prevalent in power generation, aerospace, and advanced manufacturing industries [4,5].

High-pressure compressor blades are critical components in aero-engine systems, operating under extreme conditions of high rotational speeds, elevated temperatures, and severe dynamic loading. These operating conditions make the blades highly susceptible to vibration-induced failures such as fatigue, resonance, and excessive dynamic deflection. The 3D model and cross-sectional beam model of compressor blade are illustrated in Fig. 1

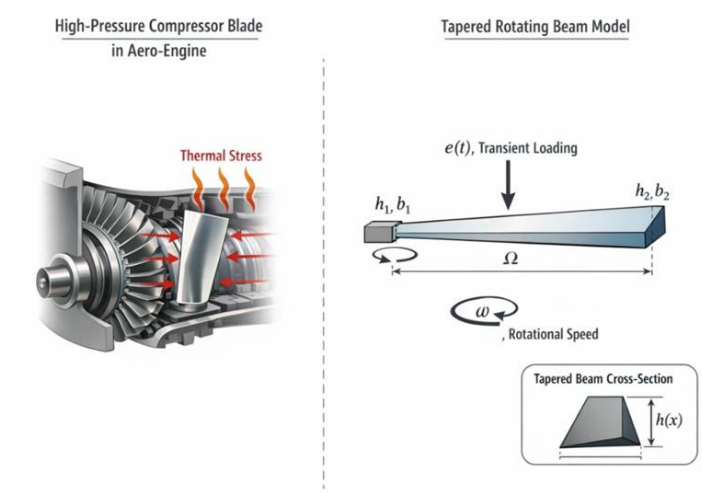

Figure 1. Schematic 3D model of compressor blade

The dynamic performance of compressor blades is significantly influenced by centrifugal stiffening due to rotation, geometric variations along the blade length, and thermally induced stresses. Accurate prediction of vibration characteristics is therefore essential to ensure structural integrity, reliability, and safe operation of aero-engine compressors.

In many analytical and numerical studies, compressor blades are idealized as rotating beams to simplify the formulation while retaining the essential dynamic behavior. Among various geometric configurations, tapered beam models provide a more realistic representation of actual compressor blade geometry compared to uniform cross-section models.

Although several studies have reported the free vibration characteristics of rotating blades, limited attention has been given to the transient dynamic response under combined thermo-rotational effects. Furthermore, the coupled influence of taper ratio, aspect ratio, temperature rise, and rotational speed on blade dynamics remains inadequately explored.

In recent years, numerical simulation techniques have been widely employed to analyze the vibration behavior of rotating blades; however, repeated simulations for design optimization are computationally expensive. Intelligent surrogate models such as artificial neural networks offer an efficient alternative for predicting dynamic responses and facilitating optimization.

Motivated by these observations, the present work focuses on the numerical investigation of free vibration and transient response of a thermally stressed tapered rotating high-pressure compressor blade, with the aim of improving its dynamic performance through efficient optimization techniques.

High-temperature environments introduce significant complexities in the vibration analysis of rotating structures. Thermal gradients generate thermal stresses, alter material properties such as stiffness and damping, and may induce thermal buckling or post-buckling phenomena, all of which can substantially influence the dynamic response of rotating components. Extensive research has been conducted on the vibration behavior of rotating structural components subjected to various mechanical and thermal loading conditions. Malgaca and Uyar [6] investigated the vibration characteristics of laminated carbon-fiber box beams with rectangular cross-sections and examined the effects of link and joint flexibility on their dynamic performance. Parida and Mohanty [7] studied the free vibration behavior of rotating functionally graded (FG) plates under non-uniform thermal environments and demonstrated the significant influence of temperature on vibration characteristics.

Similarly, Chen et al. [8] analyzed the vibration response of rotating pre-twisted functionally graded sandwich blades operating under thermal loading conditions and reported notable changes in dynamic behavior due to material gradation and temperature variation. Zhang and Li [9] investigated the nonlinear forced vibration response of pre-deformed rotating blades subjected to distributed gas pressure and thermal gradients, highlighting the complex interaction between thermal and aerodynamic loads.

Several analytical and numerical approaches have been proposed to evaluate the static and dynamic behavior of thermally loaded rotating FG structures. Shahba et al. [10] employed the finite element method to study the free vibration characteristics of centrifugally stiffened conical FG beams. Entezari et al. [11] investigated stress distributions in rotating disks and rotors with variable thickness using a refined finite element formulation. Heydarpour et al. [12] analyzed the thermoelastic response of rotating functionally graded cylindrical shells through the differential quadrature method. Kim et al. [13] developed coupled flapwise–chordwise equations of motion for rotating beams using Hamilton's principle. More recently, Wang et al. [14] proposed dynamic models for elastically constrained rotating beams based on both Euler–Bernoulli and Timoshenko beam theories. Mazanoglu and Guler [15] employed the Rayleigh–Ritz method to investigate flapwise and chordwise vibrations of tapered rotating beams under classical boundary conditions. Dangarwala and Nagendra Gopal [16] utilized Bardell polynomials within a Ritz-based element formulation to study the free vibration behavior of rotating non-uniform cantilever beams.

2. Mathematical Model

2.1. Materials Model

The schematic of functionally graded rotating beam with length L, thickness h is shown in Fig. 2. The beam is exposed to uniform thermal environment.

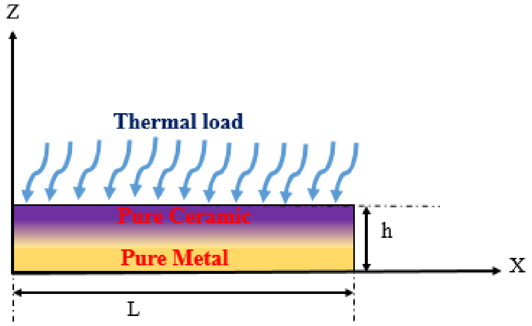

Figure 2 Schematic of thermally stressed FG beam

The functionally graded beam is graded in thickness direction as SiC as ceramic and Aluminium as a metal. The upper phase contains pure ceramic and the lower phase contains pure metal. The effective material properties like elastic modulus, density and thermal expansion coefficient are obtained using the power law, which is expressed as:

$$P(z) = P_c(z) + (P_m(z) - P_c(z))\left(0.5 + \frac{z}{h}\right)^{n_z} \tag{1}$$

Where $P(z)$, $P_c(z)$ and $P_m(z)$ represent the effective material property, ceramic material and metal, respectively. The grading index in thickness direction is indicated as n_z.

2.2 Dynamic Model

Let transverse displacement w(x,t) and cross-section rotation φ(x,t) be the primary fields in the beam. The beam is also subjected to thermal load and rotational effect, therefore total axial stress is $N_{Total} = N_{th} + N_R$.
Where

$$N_{th} = E_{eff}\,\alpha_{eff} A \Delta T \tag{2a}$$

$$N_R = \int_x^L \rho_{eff} A\, \Omega^2(s) ds = \frac{1}{2}\rho_{eff} A\, \Omega^2(L^2 - x^2) \tag{2b}$$

The governing equation of motion including thermal and rotational effect using Timoshenko beam theory can be obtained as:

$$\rho_{eff} A \frac{\partial^2 w}{\partial t^2} - \frac{\partial}{\partial x}\left[k_s G_{eff} A\left(\varphi - \frac{\partial w}{\partial x}\right)\right] - \frac{\partial}{\partial x}\left(N_{Total}\frac{\partial w}{\partial x}\right) = q(x,t) \tag{3a}$$

$$I_r \frac{\partial^2 \varphi}{\partial t^2} - \frac{\partial}{\partial x}\left(E_{eff}\, I \frac{\partial \varphi}{\partial x}\right) + \left[k_s G_{eff} A\left(\varphi - \frac{\partial w}{\partial x}\right)\right] = m(x,t) \tag{3b}$$

Where $q(x,t)$ is transverse distributed load, I_r indicates rotary inertia per unit length and k_s is shear correction factor. The governing equations are converted to their weak form and discretized using standard Timoshenko beam finite elements. Assembly yields the semi-discrete system without external load as:

$$M\ddot{d} + (K + K_G)d = 0 \tag{4}$$

In which M, K and K_G are the mass and stiffness matrices. The global DOF vector is represented as d. The above equation is solved to obtain the eigen value and eigen vector.

2.3 Neural Network Model

A feed-forward neural network maps an input vector x to an output y through a series of weighted transformations. For a single hidden layer network, the mathematical representation can be written as:

$$y_h = f_1(W_1 x + b_1) \tag{5}$$

$$y_o = f_2(W_2 x + b_2) \tag{6}$$

Where

W_1, W_2 are weight matrices, b_1, b_2 are bias vectors, f_1 is the hidden layer activation function and f_2 is the output activation function. The training objective is to minimize the prediction error:

$$min_{W,b} \left\| y_{pred} - y_{target} \right\|^2 \tag{7}$$

3. Results and Discussions:

3.1 FE simulation results

Fig. 3 illustrated the variation of natural frequency of rotating beam with different temperature change and FG material compositions. As the temperature rises from 50 °C to 300 °C, the stiffness of both SiC and Al reduces due to temperature-dependent degradation of the elastic modulus, and the accompanying thermal expansion induces compressive thermal stresses. These combined effects significantly lower the effective bending rigidity of the beam, resulting in a drop in natural frequency. The results also shows that the rate of reduction is influenced by the FG material composition: beams with lower power-law indices (ceramic-rich) maintain higher natural frequencies and exhibit better thermal stability because SiC retains stiffness more effectively at elevated temperatures compared to aluminium. The nonlinear decrease at higher thermal levels further emphasizes that FGMs behave differently under moderate and high heat environments.

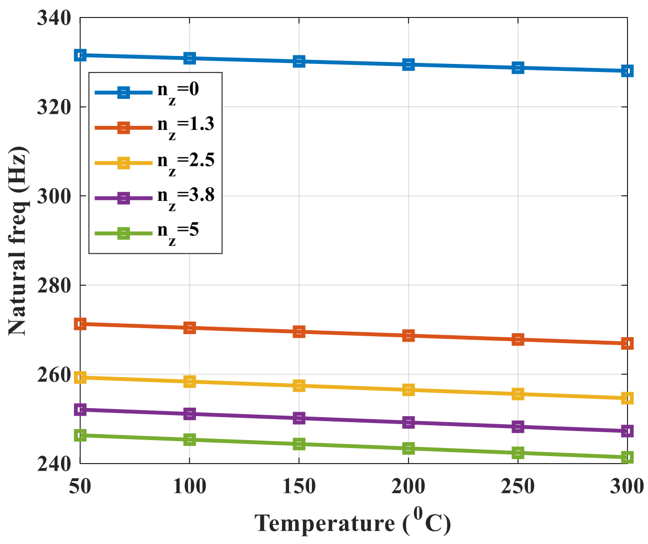

Figure 3. Variation of natural frequency of FG rotating beam for different temperature change and gradation index

Overall, the figure demonstrates that temperature is a dominant parameter in the dynamic behaviour of rotating FGM beams, and using a ceramic-rich gradient helps preserve structural stiffness and vibration resistance under thermal loading.

Similarly, the effect of rotational speed of high compressor blade on vibration response of FG beam is shown in Fig. 4. As the rotational speed increases (from 500 rad/s to 2000rad/s), the natural frequency rises due to the centrifugal stiffening effect, which introduces additional axial tension along the beam length.

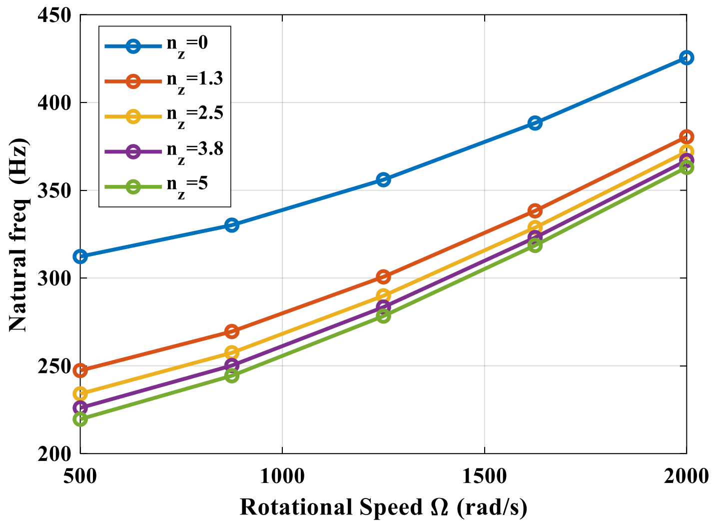

Figure 4. Variation of natural frequency of FG rotating beam for different rotational speed and gradation index

This rotationally induced tensile force effectively increases the beam's overall stiffness, thereby shifting the natural frequency to higher values, especially at higher speed ranges. However, the extent of this increase depends significantly on the FG power-law index. Beams with lower power-law indices (ceramic-rich near the surface) consistently exhibit higher natural frequencies across all rotational speeds, as the ceramic phase (SiC) provides greater rigidity and better withstands rotational stiffening. Conversely, metal-rich configurations (higher n_z) show reduced stiffness and therefore lower frequencies. The combined trend highlights that FGMs allow designers to tune dynamic performance by selecting appropriate gradation profiles.

3.2 Neural Network Predictions

After generating the FE dataset, the neural network model was trained and validated to assess its ability to predict the vibration response of thermally stressed rotating functionally graded beams. The evaluation was carried out using three key analyses: error plot, regression plot, and comparative analysis with FE results.

The error plot as shown in Fig.5 illustrates the difference between the neural network predictions and the corresponding FE results across all test samples. This plot helps identify the magnitude and distribution of prediction errors, reflecting the learning efficiency of the network. A narrow error band with small deviations indicates that the neural network accurately captures the nonlinear relationship among rotational speed, temperature gradient, material gradation, and vibration response.

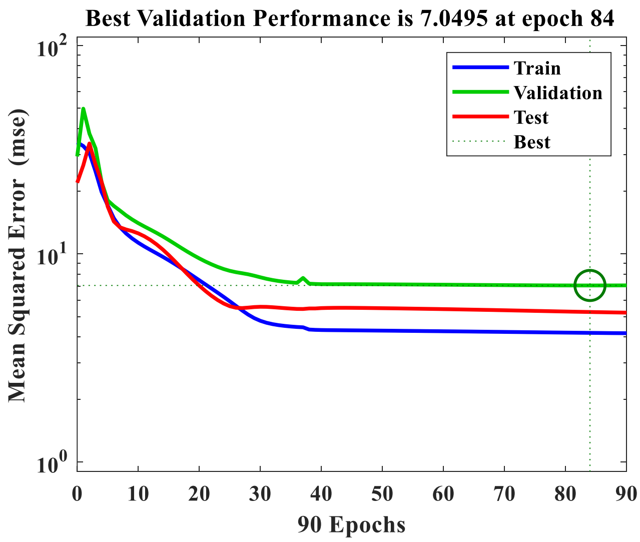

Figure 5. MSE error plot

The performance of the neural network was further examined using the regression plots obtained for the training, validation, and testing datasets as represented in Fig 6.

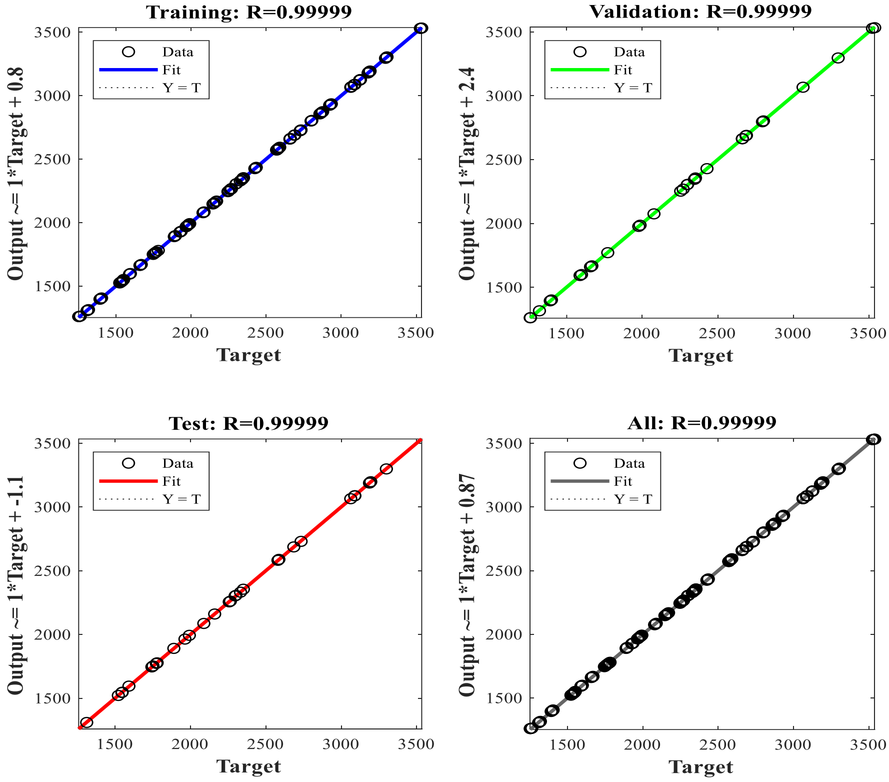

Figure 6 Performance of feed-forward neural network

These plots illustrate the relationship between the network outputs and the corresponding FE targets for each stage of the learning process. A regression line close to the ideal 45° diagonal and correlation coefficients approaching unity ($R \approx 1$) indicate strong predictive capability. Additionally, the combined regression plot confirms that the network maintains consistent accuracy across all data subsets, demonstrating effective learning, minimal overfitting, and reliable generalization. The training, validation, and testing error curves also show smooth convergence, further verifying the robustness and stability of the developed neural network model. To assess the accuracy of the developed neural network model, its predictions are directly compared with the finite element results for selected combinations of temperature levels, rotational speeds, and power-law indices. The comparative results presented in Table 1 indicate excellent agreement between the two datasets. In most cases, the prediction error remains below 5%, confirming that the NN model successfully captures the vibration behavior of the rotating FGM beam with high fidelity. This close correlation validates the robustness and reliability of the proposed neural network framework for fast prediction, sensitivity studies, and parametric analysis, significantly reducing the computational burden associated with repeated FE simulations.

Table 1. Comparison of natural frequencies with FE results and NN predictions

Input parameters			Output parameters		Error
n_z	T (°C)	Ω (rad/s)	NN Output	FE output	(%)
1.5	25	800	296.79	283.12	4.60
2.5	35	1500	400.16	391.95	2.05
0.5	105	1400	431.42	410.97	4.74
0.25	120	750	351.00	335.31	4.47
0.3	235	560	327.01	318.15	2.70
4	220	1750	438.44	425.38	2.97
4.6	230	1440	373.17	368.25	1.31

4. Optimization Study

4.1 Optimization Formulation

From the parametric analysis, it is evident that the natural frequency, dynamic response, of the rotating structure are significantly affected by variations in material and geometric parameters. Since these performance measures are often conflicting in nature, a multi-objective optimization framework is required. In the present study, the objective is to maximize the fundamental natural frequency (F_1) while minimizing the maximum dynamic response amplitude (F_2).

To handle this multi-objective problem, a weighted sum approach is adopted, wherein multiple objectives are combined into a single scalar objective function. Accordingly, the optimization problem is formulated as:

$$\text{Minimize } F(X) = w_1 \frac{1}{F_1(X)} + w_2 F_2(X)$$
$$\text{Subject to } X \in \{X_{min}, X_{max}\} \tag{8}$$

where X = [n_z, Ω,T,L/b] is set of design variables, while w_1, and w_2 denote the weighting factors associated with the natural frequency and dynamic responses. The term X_{min} and X_{max} correspond to the lower and upper bounds imposed on the design variables. Table 2 shows the three levels for each variable considered for further study.

Table 2. Design variables and levels

Symbol	Design variables	Level 1	Level 2	Level 3
A	Grading index in length direction (n_z)	0	5	10
B	Rotational speed (Ω)	0	1000	2000
C	Temperature (T)	0	100	300
D	Aspect ratio (L/b)	5	15	25

The sequence of four-factors and three-level design is shown in Table 3. The L_9 orthogonal array is used to collect the output data.

Table 3 The L_9 orthogonal array data

Exp. No.	n_z	Ω	T	L/b	Natural frequency	Dynamic response (10^{-5}) m
1	1	1	1	1	305.28	1.296
2	1	2	2	2	338.65	1.307
3	1	3	3	3	423.89	1.333
4	2	1	2	3	207.68	3.023
5	2	2	3	1	251.98	3.025
6	2	3	1	2	365.03	2.965
7	3	1	3	2	183.77	3.796
8	3	2	1	3	242.78	3.538
9	3	3	2	1	353.33	3.621

In surrogate model framework, the optimized parameters can be obtained by implementing the searching ability of the optimization algorithm using the trained neural network function evaluations. Artificial neural networks (ANNs) are widely used to simulate complex problems. Multilayer Perceptron (MLP) is a famous feed-forward ANN architecture that connects the inputs and outputs through hidden layers. All these neurons are connected by synoptic strengths called weights, which take part in the network's learning process . In typical single hidden layer structure, the hidden layer outputs are expressed as a function of weighted sum of all inputs received at different nodes as:

$$H = f_1(W_I X_I + b_I) \tag{9}$$

Here, f_1 is the hidden layer transfer function, W_I is the weights in the input layer, X_I is the inputs of the input layer, and b_I is the bias vector in the hidden layer. Similarly, the actual outputs at the output-layer can be expressed as:

$$Y = f_2(W_o H_o + b_o) \tag{10}$$

Here, f_2 is the output layer transfer function, W_o is the weights in the output layer, and b_o is the biases in the output layer. The expression for H_o in terms of sigmoid function is written as:

$$H_o = \frac{1}{(1+exp(-H))} \tag{11}$$

By providing a set of inputs and corresponding outputs, the weights are adjusted after series of epochs by minimizing the mean square output error using backpropagation learning rule. The representation of the neuron of the neural network for the present study are shown in Fig. 7.

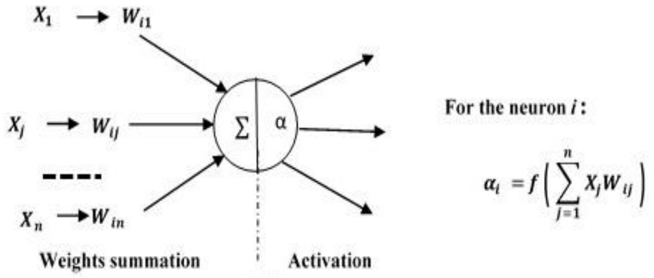

Figure 7. Artificial neuron

Higher performance and accuracy can be achieved when the error is as low as possible and the regression coefficient value (R^2) becomes close to 1. The minimum number of hidden layer neurons is considered according to the rule h = $\sqrt{m+n}$, where *m* and *n* are number of input and output neurons respectively.

Weights and biases of all the layers of neurons are combined with transfer functions of MLP model to achieve an equation pattern for optimization. All the 27 experimental results are used for training the model. The predicted mean-square error values obtained for different number of hidden layer neurons is depicted in Table 4. It is seen that 8 neuron configuration minimizes the error in better way for same 1000 epochs learning cycle and is considered further in function evaluation process.

Table 4. Mean Square Error for different hidden layer nodes

S.No.	Hidden Neurons	Mean square error (MSE)
1	2	0.0003073
2	4	0.000253
3	6	11.028×10^{-6}
4	8	1.6715×10^{-13}

The regression map and performance curve are shown in Fig. 8 (a) and (b), respectively. It can be noticed that the regression coefficient is found very close to one.

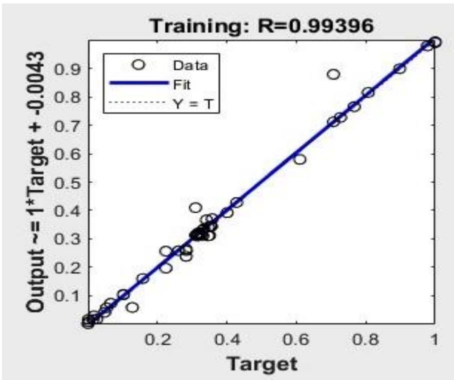

(a)

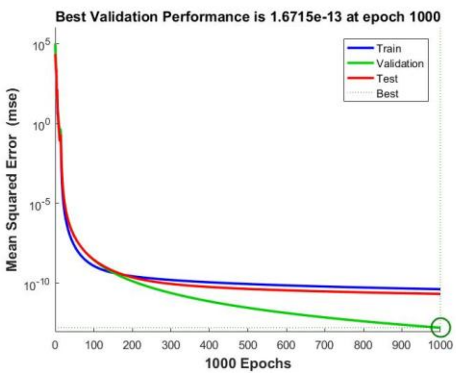

(b)

Figure 8 (a). Regression map (b) Performance curve

4.2 Particle Swarm Optimization Scheme (PSO algorithm)

Particle Swarm Optimization (PSO) is a population-based stochastic optimization technique inspired by the social behavior of bird flocking and fish schooling. PSO is widely used for solving nonlinear, multi-modal, and multi-objective optimization problems, especially in engineering applications like structural optimization, MEMS design, vibration control, and machine learning.

In PSO, a group of candidate solutions called *particles* move through the search space to find the optimal solution. Each particle adjusts its position based on:

- Its own experience (personal best)
- The experience of neighbouring particles (global best)

This collective intelligence helps the swarm converge toward the optimal solution efficiently.

The mathematical expressions for this algorithm is described here. Each particle is characterized by:

Position vector: $x_i = (x_{i1,}\ x_{i2,}\ x_{i3,}\ \dots\dots\dots..x_{id,}\ )$

Velocity vector: $v_i = (v_{i1,}\ v_{i2,}\ v_{i3,}\ \dots\dots\dots..v_{id,}\ )$

The velocity and position updates are given by:

$$v_i^{k+1} = w.v_i^k + c_1.r_1.(pbest_i - x_i^k) + c_2.r_2.(gbest_i - x_i^k) \tag{12}$$

$$x_i^{k+1} = x_i^k + v_i^{k+1} \tag{13}$$

Where:

- w = inertia weight
- c_1 and c_2= cognitive and social acceleration coefficients
- r_1 and r_2= random numbers in [0,1]
- $pbest_i$ = best position of particle iii
- $gbest_i$e = global best position among all particles

The steps of the PSO algorithm can be written as:

1. Initialize a swarm of particles with random positions and velocities.
2. Evaluate the fitness function for each particle.
3. Update personal best ($pbest_i$) if current fitness is better.
4. Update global best ($gbest_i$) among all particles.
5. Update velocity and position using the governing equations.
6. Repeat steps 2–5 until convergence or maximum iterations are reached.

4.3 Optimization Results

The PSO Algorithm successfully identified the optimal combination of design variables after 229 iterations. The optimum values of the design parameters were obtained as n_z =0.03, Ω =1999.99rpm, T =15.9^{0}C, and L/b = 5. The convergence plot is shown in Fig. 9.

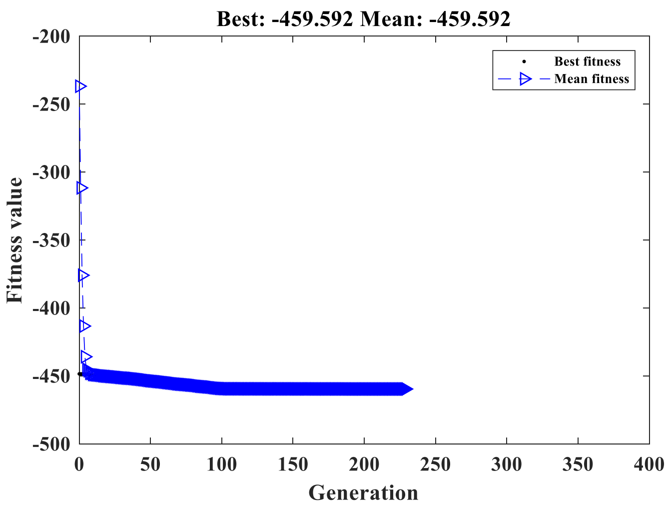

Figure 9. Convergence of Natural frequency

At this optimal configuration, the natural frequency increased significantly to 459.52 Hz compared to the initial maximum value of 423 Hz. This 10 % improvement demonstrates the effectiveness of the PSO-based optimization approach in enhancing the dynamic performance of the structure by efficiently exploring the design space and identifying the most favourable parameter combination.

Similarly, for the minimization of dynamic deflection, the PSO algorithm converged to the optimal solution after 51 iterations. The optimum design variables were obtained as n_z = 1.127, Ω = 1941.75rpm, T = 26^{0}C, and L/b = 5. The obtained results indicate that the selected optimization algorithm efficiently searched the design space and rapidly converged toward the minimum dynamic deflection configuration within a relatively smaller number of iterations as shown in Fig 10. This demonstrates the capability of the optimization algorithm in improving the structural dynamic response and achieving enhanced vibration suppression characteristics.

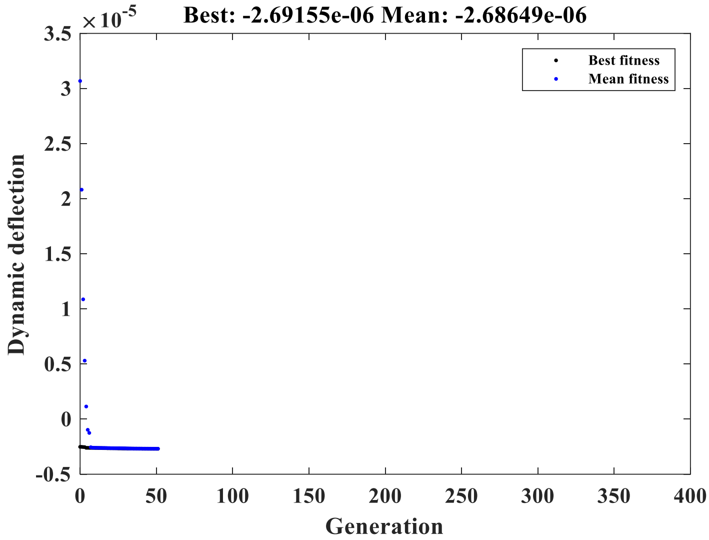

Figure 10. Convergence of dynamic deflection

Finally, the multi-objective optimization was carried out using the multi-objective particle swarm optimization algorithm (MOPSO) to simultaneously maximize the natural frequency and minimize the dynamic deflection of the structure. Based on the obtained Pareto optimal solutions, the best 10 design combinations as listed in Table 5, are selected considering the trade-off between higher natural frequency and lower deflection. These solutions represent the most efficient configurations among all feasible designs generated during the optimization process.

Table 5. Best 10 non-dominating optimal solution

S.N.	n_z	Ω	T	L/b	F_1	F_2
1	1.922	1580.637	28.358	2.469	335.251	2.84E-06
2	2.138	1248.844	18.208	3.494	286.209	4.13E-05
3	1.881	622.83	12.72	2.544	242.569	2.02E-05
4	1.666	475.664	16.024	3.383	308.61	1.49E-05
5	2.407	679.115	25.936	2.711	454.992	2.10E-05
6	3.323	1069.433	26.086	2.574	444.627	3.43E-05
7	1.999	100.001	28.165	3.747	421.76	7.84E-07
8	1.516	764.912	17.58	1.845	375.014	2.47E-05
9	0.191	1994.697	18.737	1.079	458.163	6.82E-05
10	0.736	686.511	17.695	2.675	457.022	2.20E-05

The Pareto front is plotted in Fig 11, to illustrate the relationship between the conflicting objective functions. The generated Pareto curve clearly demonstrates that an improvement in natural frequency is generally accompanied by an increase in dynamic deflection, indicating the inherent trade-off between stiffness enhancement and deformation control. Therefore, the Pareto front provides a set of optimal compromise solutions from which the designer can select the most suitable configuration according to practical engineering requirements and performance priorities.

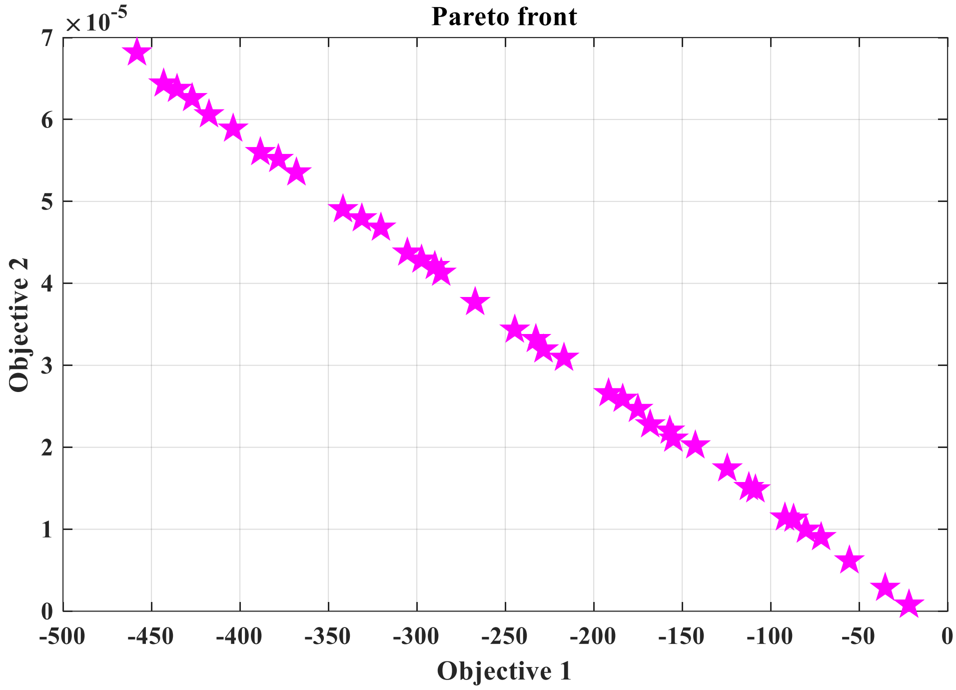

Figure 11. Pareto front for non-dominating solutions

5. Conclusion

A comprehensive numerical and computational framework was developed to evaluate the dynamic characteristics of the rotating beam with improved accuracy and computational efficiency. The following conclusions are drawn:

- The effective material properties of the functionally graded beam were evaluated using a power-law distribution through the thickness direction. Temperature-dependent material properties were incorporated to realistically capture the degradation in stiffness under elevated thermal conditions. The developed formulation successfully included the combined influence of centrifugal stiffening due to rotation and thermal softening due to temperature rise.
- The finite element-based numerical model was implemented to evaluate the free vibration characteristics of the rotating beam. The obtained results demonstrated that the rotational speed significantly influences the structural stiffness and natural frequency. It was observed that an increase in rotational speed enhances the natural frequency because of the centrifugal stiffening effect generated during rotation.
- In contrast, thermal loading reduces the effective stiffness of the beam, thereby decreasing the natural frequency values. The study also revealed that the material grading index plays an important role in controlling the dynamic behavior of the structure. A lower power-law index, corresponding to a higher ceramic content, considerably improved the stiffness characteristics and enhanced the vibration resistance of the beam.
- A detailed parametric investigation was carried out to study the effects of rotational speed, temperature rise, and grading index on the vibration response. The results confirmed that the combined thermo-rotational environment has a substantial impact on the dynamic stability and structural performance of rotating blades.
- Therefore, proper selection of material composition and geometric parameters is essential for achieving improved vibration characteristics in high-speed rotating applications such as turbine blades, compressor blades, aerospace structures, and micro-scale rotating systems.
- To reduce computational effort and improve prediction efficiency, an Artificial Neural Network (ANN)-based surrogate prediction model was developed using FE-generated datasets. The neural network model was successfully trained and validated for predicting the natural frequency of the rotating beam.
- Regression analysis, comparison plots, and error evaluation confirmed that the ANN model can accurately reproduce the FE results with high prediction capability and minimal computational time. The developed surrogate model can therefore serve as an efficient alternative for rapid dynamic response estimation and design optimization studies.

- Further, Particle swarm optimization algorithm (PSO)-based optimization was performed to identify the optimal design parameters for improving the dynamic performance of the rotating structure. The optimization results showed a significant enhancement in the natural frequency compared to the initial design configuration. The PSO efficiently converged toward the optimal solution by exploring the design space and selecting the most favourable parameter combinations.
- Subsequently, multi-objective optimization using the Multi-objective particle swarm optimization algorithm (MOPSOA) was carried out to simultaneously maximize the natural frequency and minimize the dynamic deflection. The Pareto optimal solutions obtained from the optimization process clearly demonstrated the trade-off relationship between stiffness enhancement and deformation control. From the Pareto front, the best ten optimal design combinations were selected to provide suitable compromise solutions for practical engineering applications. The developed optimization framework therefore offers an effective methodology for the design and performance enhancement of rotating functionally graded blade structures operating under thermo-mechanical environments.

References

[1] S. Hussain, W. A. W. Ghopa, S. S. K. Singh, A. H. Azman, and S. Abdullah, “Experimental and numerical vibration analysis of octet-truss-lattice-based gas turbine blades,” *Metals*, vol. 12, Art. no. 340, 2022, doi: 10.3390/met12020340.

[2] N. Liu, H. Mo, H. Wang, A. Huang, J. Zhang, Z. Wang, *et al*., “Simulation and experimental analysis of diesel engine shafting angular misalignment for online fault detection,” *Measurement*, vol. 252, Art. no. 117406, 2025, doi: 10.1016/j.measurement.2025.117406.

[3] J. Pacheco-Chérrez, D. Cárdenas, A. Delgado-Gutiérrez, and O. Probst, “Operational modal analysis for damage detection in a rotating wind turbine blade in the presence of measurement noise,” *Composite Structures*, vol. 321, Art. no. 117298, 2023, doi: 10.1016/j.compstruct.2023.117298.

[4] S. Shah, M. C. Luintel, and S. Bhattrai, “Comprehensive review on vibration response and dynamic analysis of rotating blades under thermal environment,” *International Journal of Dynamics and Control*, vol. 13, 2025, doi: 10.1007/s40435-025-01776-6.

[5] U. K. Kar and J. Srinivas, “Vibration analysis of bi-directional FG-GNPs reinforced rotating micro-beam under thermo-mechanical loading,” *Materials Today: Proceedings*, vol. 78, pp. 752–759, 2022, doi: 10.1016/j.matpr.2022.10.227.

[6] L. Malgaca and M. Uyar, “Hybrid vibration control of a flexible composite box cross-sectional manipulator with piezoelectric actuators,” *Composites Part B: Engineering*, vol. 176, Art. no. 107278, 2019, doi: 10.1016/j.compositesb.2019.107278.

[7] S. Parida and S. C. Mohanty, “Free vibration analysis of rotating functionally graded material plate under nonlinear thermal environment using higher order shear deformation theory,” *Proceedings of the Institution of Mechanical Engineers, Part C: Journal of Mechanical Engineering Science*, vol. 233, pp. 2056–2073, 2019, doi: 10.1177/0954406218777535.

[8] Y. Chen, T. Ye, G. Jin, S. Li, and C. Yang, “Vibration analysis of rotating pretwist FG sandwich blades operating in thermal environment,” *International Journal of Mechanical Sciences*, vol. 205, Art. no. 106596, 2021, doi: 10.1016/j.ijmecsci.2021.106596.

[9] B. Zhang and Y. Li, “Nonlinear vibration of rotating pre-deformed blade with thermal gradient,” *Nonlinear Dynamics*, vol. 86, pp. 459–478, 2016, doi: 10.1007/s11071-016-2900-4.

[10] A. Shahba, R. Attarnejad, and H. Zarrinzadeh, “Free vibration analysis of centrifugally stiffened tapered functionally graded beams,” *Mechanics of Advanced Materials and Structures*, vol. 20, no. 4, pp. 331–338, 2013, doi: 10.1080/15376494.2011.627634.

[11] A. Entezari, M. A. Kouchakzadeh, E. Carrera, and M. Filippi, “A refined finite element method for stress analysis of rotors and rotating disks with variable thickness,” *Acta Mechanica*, vol. 228, pp. 575–594, 2017, doi: 10.1007/s00707-016-1727-x.

[12] Y. Heydarpour, P. Malekzadeh, M. R. Golbahar Haghighi, and M. Vaghefi, “Thermoelastic analysis of rotating laminated functionally graded cylindrical shells using layerwise differential quadrature method,” *Acta Mechanica*, vol. 223, pp. 81–93, 2012, doi: 10.1007/s00707-011-0551-6.

[13] H. Kim, H. H. Yoo, and J. Chung, “Dynamic model for free vibration and response analysis of rotating beams,” *Journal of Sound and Vibration*, vol. 332, no. 23, pp. 5917–5928, 2013, doi: 10.1016/j.jsv.2013.06.004.

[14] L. Wang, Z. Su, and L. Wang, “In-plane vibration analysis of rotating beams with elastic restraints,” *Journal of Vibration and Control*, vol. 29, pp. 1484–1497, 2023, doi: 10.1177/10775463211064690.

[15] K. Mazanoglu and S. Guler, “Flap-wise and chord-wise vibrations of axially functionally graded tapered beams rotating around a hub,” *Mechanical Systems and Signal Processing*, vol. 89, pp. 97–107, 2017, doi: 10.1016/j.ymssp.2016.07.017.

[16] R. K. Dangarwala and K. V. Nagendra Gopal, “Coupled free vibration analysis of rotating non-uniform cantilever beams by an element-wise Ritz method using local hierarchical functions,” *Computers & Structures*, vol. 288, Art. no. 107133, 2023, doi: 10.1016/j.compstruc.2023.107133.

[17] U. K. Kar and J. Srinivas, “Stability and vibration control of electrostatically excited functionally graded microresonator using nonlinear observer based sliding mode controller,” *Physica Scripta*, vol. 99, 2024, doi: 10.1088/1402-4896/ad79ac.

[18] J. Wang, W. Chen, X. Wang, and N. Liu, “Stability analysis system of functionally graded material beams based on machine learning,” *Procedia Computer Science*, vol. 262, pp. 1002–1010, 2025, doi: 10.1016/j.procs.2025.05.135.

[19] F. Zheng, R. Duan, X. Chen, and Y. Lu, “Machine learning, numerical, and analytical approaches for vibration prediction of porous gradient piezoelectric beams under traveling force,” *Measurement*, vol. 245, Art. no. 116565, 2025, doi: 10.1016/j.measurement.2024.116565.

[20] S. Yildirim, “Free vibration of axially or transversely graded beams using finite-element and artificial intelligence,” *Alexandria Engineering Journal*, vol. 61, pp. 2220–2229, 2022, doi: 10.1016/j.aej.2021.07.004.

[21] M. Siavashi, M. Dardel, and M. H. Pashaei, “Nonlinear stability and vibration analysis of fluid-conveying nanochannel scroll shells using an adaptive neuro-fuzzy inference system,” *Thin-Walled Structures*, vol. 218, Art. no. 113931, 2026, doi: 10.1016/j.tws.2025.113931.

[22] L. Yang, C. Xin, Z. Wang, X. Yu, I. Hajirasouliha, and W. Feng, “Seismic resilience analysis of high-speed railway tunnels across fault zones using ensemble learning approach,” *Underground Space*, 2025, doi: 10.1016/j.undsp.2025.04.011.

[23] H. Shi, “A parametric blade design method for high-speed axial compressor,” *Aerospace*, vol. 8, Art. no. 271, 2021, doi: 10.3390/aerospace8090271.

[24] U. K. Kar and J. Srinivas, “Frequency analysis and shock response studies in bidirectional functionally graded microbeam with thermal effects,” *Journal of the Brazilian Society of Mechanical Sciences and Engineering*, vol. 44, 2022, doi: 10.1007/s40430-022-03615-7.